Segregation patterns in three-dimensional granular flows

Mengqi Yu,[1] Julio M. Ottino,[1,2,3] Richard M. Lueptow,[2,1,3,*] and Paul B. Umbanhowar[2]
[1]*Department of Chemical and Biological Engineering, Northwestern University, Evanston, Illinois 60208, USA*
[2]*Department of Mechanical Engineering, Northwestern University, Evanston, Illinois 60208, USA*
[3]*Northwestern Institute on Complex Systems (NICO), Northwestern University, Evanston, Illinois 60208, USA*

(Received 19 March 2022; accepted 20 July 2022; published 11 August 2022)

Flow of size-bidisperse particle mixtures in a spherical tumbler rotating alternately about two perpendicular axes produces segregation patterns that track the location of nonmixing islands predicted by a dynamical systems approach. To better understand the paradoxical accumulation of large particles in regions defined by barriers to transport, we perform discrete element method (DEM) simulations to visualize the three-dimensional structure of the segregation patterns and track individual particles. Our DEM simulations and modeling results indicate that segregation pattern formation in the biaxial spherical tumbler is due to the interaction of size-driven radial segregation with the weak spanwise component of the advective surface flow. Specifically, we find that after large particles segregate to the surface, slow axial drift in the flowing layer, which is inherent to spherical tumblers, is sufficient to drive large particles across nominal transport barriers and into nonmixing islands predicted by an advective flow model in the absence of axial drift. Axial drift alters the periodic dynamics of nonmixing islands, turning them into "sinks" where large particles accumulate even in the presence of collisional diffusion. Overall, our results indicate that weak perturbation of chaotic flow has the potential to alter key dynamical system features (e.g., transport barriers), which ultimately can result in unexpected physical phenomena.

DOI: 10.1103/PhysRevE.106.024902

I. INTRODUCTION

Segregation, or demixing, in flowing granular materials occurs in many industrial settings, including the processing, blending, transport, and handling of pharmaceutical, chemical, and construction materials in granular or powder form. In shearing flows, granular materials segregate when the component particles differ in physical properties, most commonly size or density [1,2]. The tendency to segregate is countered by collisional diffusion driven by particle collisions, which can lead to remixing. Experiments and modeling methods have been developed to understand the interaction of these elements in various prototypical geometries [3,4]. Here we consider segregation pattern formation in a spherical tumbler where the nominal advection field is periodic, but where interactions with particle segregation can lead to a sensitive dependence on flow conditions.

Most segregation studies in tumbler flows focus on quasi-two-dimensional (2D) geometries where the axial dimension is small compared to the radial dimension; this geometry results in an effectively 2D velocity field. In quasi-2D tumblers rotating in the cascading regime [5,6], a thin flat free-surface layer of particles flows above a nominally fixed bed, or "bulk," of particles in solid-body rotation with the tumbler. Segregation patterns for a size-bidisperse mixture of particles in quasi-2D tumblers correspond to the dynamics of the system. In a typical quasi-2D circular tumbler rotating at constant speed and half-filled with a size-bidisperse particle mixture, segregation in the flowing layer leads to a radial segregation pattern where large particles migrate to the tumbler periphery, leaving a core of small particles at the center within one to two revolutions [7–11]. This process is well understood and can be accurately modeled using a continuum transport model [3,4,12]. When the rotation speed is slowed or modulated, or the tumbler is not half full, the boundary between large particles on the periphery and the small-particle core develops a multilobed structure, which can coarsen at high fill-levels [13–19]. Similarly, lobed patterns are observed in quasi-2D tumblers with polygonal cross-sections, due to the time-periodicity of the flow induced by rotation of the polygonal geometry. These lobed patterns are closely related to the unstable manifolds of the associated dynamical system [14,20].

Though quasi-2D geometries have provided a useful avenue for study, tumblers in practical applications are almost always three-dimensional (3D). Here we consider a 3D tumbler geometry in which the underlying flow dynamics are chaotic [21–23], which leads to complex interactions between advection, segregation, and collisional diffusion. In particular, we consider a segregating granular mixture in what is arguably the simplest nontrivial 3D geometry, a spherical tumbler with periodic flow dynamics, specifically the biaxial spherical tumbler (BST) flow. The tumbler is half-filled with a size-bidisperse noncohesive granular material and rotated alternately about two horizontal axes by rotation angles (θ_z, θ_x) beyond the angle of repose. The choice of axes and rotation angles is termed a protocol. Here we restrict our study to

*Corresponding author: r-lueptow@northwestern.edu

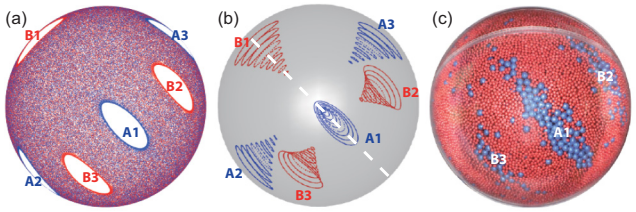

FIG. 1. Flow and segregation structures for the (57°, 57°) protocol. (a) Poincaré section from a continuum model (CM) simulation of a half-full spherical tumbler at $r = 0.95$. (b) 3D nonmixing KAM tubes visualized by transport barriers from CM for $0.55 \leqslant r \leqslant 0.95$ in radial increments of 0.05. The six conelike KAM tubes (A1–A3 and B1–B3) are period-3. The dashed white line indicates an intersecting plane used for analysis in Sec. II B. (c) Segregation experiment in a half-full 7 cm radius spherical tumbler with fraction $f = 0.05$ large blue (shaded gray) particles and $1 - f = 0.95$ small red (gray) particles by volume after $N = 30$ iterations of the (57°, 57°) protocol with angular velocity $\omega = 2.6$ rpm. All images show the mixture-filled half of the tumbler viewed from below. Adapted with permission from [32].

rotations about orthogonal axes, although nonorthogonal axes can produce similar flow structures [24].

Mixing dynamics in the BST are richly complex, even in the simpler case of a nonsegregating monodisperse (versus size disperse) granular material. In the monodisperse case, and for certain biaxial spherical tumbler protocols, some particles are trapped for many iterations, N, of the protocol in periodic "nonmixing regions," while particles outside of these regions mix chaotically [25]. At what is likely the most fundamental level, the mixing dynamics of the BST can be viewed as a cutting-and-shuffling operation described by the mathematics of piecewise isometries (PWI) [21,25–29]. Essentially, each change in rotation axis "cuts" the material, while each rotation "shuffles" it to a different location. The PWI approach identifies the potential for nonmixing regions (i.e., regions that are never cut) [21,25,26,29] and invariant ergodic subsets that can result in barriers to mixing [30], but the details of these predictions are altered by the finite thickness of the flowing layer in any physical realization of the BST [21,23,25,26]. However, the finite thickness flowing layer can be modeled using a continuum description with a time-periodic 3D velocity field [22,23,25] (see Appendix A). This continuum model, or CM, is directly applicable to the description of monodisperse flows, which, by definition, do not exhibit segregation.

An example of flow structures predicted by the CM is shown in Fig. 1(a) as viewed from below for multiple applications of the rotation protocol $(\theta_z, \theta_x) = (57°, 57°)$ at a radius of $r = 0.95$ for a unit hemisphere using a Poincaré section [31], i.e., a stroboscopic map showing the locations of all tracer points after each iteration of the protocol due to advection by the flow. The CM predicts a flow structure consisting of two groups of nonmixing islands (labeled A1–A3 and B1–B3) surrounded by a scatter of points corresponding to a single large chaotic flow region [22,23]. Within each island, tracer point trajectories are periodic and orbit around the center of the island, while outside each island, tracer point trajectories are chaotic [27]. The boundary of each island forms a transport barrier across which tracer particles do not cross in the CM model but can cross in physical flows and discrete element method (DEM) simulations due to collisional diffusion. For the (57°, 57°) protocol, the islands have period-3 orbits, meaning that they return to the same location on the hemisphere after three iterations of the tumbling protocol. (More generally, a period-n orbit returns to the same location after n iterations of the protocol.)

Since the flow is 3D, the boundaries of the nonmixing islands shown in Fig. 1(a) are the intersections of the $r = 0.95$ shell with six conelike nonmixing volumes called Kolmogorov-Arnold-Moser (KAM) tubes. Figure 1(b) [32] illustrates the cone structure by showing intersections of the KAM tubes with spherical shells over a range of radii (see the caption). Within the KAM tubes, the velocity field is fully integrable and all orbits are periodic, which is in contrast to the chaotic motion that occurs outside the KAM tubes [23]. Consequently, the surface of the KAM tube also forms a barrier to transport across which tracer particles do not cross in the CM model. For the rotation protocol $(\theta_z, \theta_x) = (57°, 57°)$, the KAM tubes are widest near the tumbler wall [corresponding to the island boundaries shown in Fig. 1(a)], and their apexes point toward the center of the spherical tumbler. For different protocols with similar nonmixing behaviors, the KAM tube shape varies with the rotation protocol and the flowing layer thickness [23]. These protocol-dependent KAM structures are also observed in an experimental study of the BST system, where an x-ray opaque tracer particle among otherwise monodisperse particles periodically appears in regions A1–A3 or B1–B3 for hundreds of consecutive iterations, occasionally jumping out and back into these period-3 nonmixing islands due, in part, to collisional diffusion [25].

In addition to nonmixing barriers bounded by KAM tubes, the CM model and experiments also produce global transport barriers that instead separate two chaotic regions [25,30]. In these cases, particles remain and mix in the half of the domain where they are located before tumbling starts. These global nonmixing structures are surprising in a tumbling system where complete mixing was originally anticipated outside of KAM tubes. The observed complexity of mixing in the BST system provides a starting point to probe into more practical aspect, namely segregation.

Returning now to the case of size-bidisperse mixtures where segregation can occur, experiments have shown that the 3D chaotic flows of the BST can form segregation patterns reflecting the underlying flow dynamics of the continuum model, i.e., large particles concentrate in and around the nonmixing regions predicted by the CM [32]. For example, an experiment tumbling a mixture with large particles [$d_L = 4$ mm, blue (shaded gray), fraction $f = 0.05$] and small particles [$d_S = 2$ mm, red (gray), fraction $1 - f = 0.95$] in an $R_o = 7$ cm spherical tumbler under the (57°, 57°) protocol results in the segregation pattern at the tumbler wall shown in Fig. 1(c) [32]. Though only a portion of the tumbler is visible due to the spherical geometry of the tumbler, it is apparent that large particles accumulate in and about nonmixing regions A1, B2, and B3 of the Poincaré section shown in Figs. 1(a) and 1(b) [32]. The curious aspect of the segregation pattern in Fig. 1(c), and the phenomenon that is the focus of this study, is that the nonmixing islands, whose perimeters are barriers to

transport in both the CM and PWI models, act as "attractors" for the large particles in a segregating size-bidisperse mixture.

Here we study how segregation patterns depend on the interplay between particle segregation and the underlying dynamical system driven by the advection field. Using DEM simulations to track each particle, we first characterize the structure of the segregation patterns in Sec. II. In Sec. III we examine how large particles cross the transport barriers surrounding nonmixing regions. Based on our findings here and previous work [25,32,33], we propose that weak axial transport of surface segregated large particles is sufficient to drive segregation pattern formation when nonmixing regions are present. To support this hypothesis, axial transport is incorporated into the CM. Results from this modified continuum model, or MCM, demonstrate that a weak perturbation to the base flow results in the accumulation of large particles in nonmixing regions predicted by the unperturbed flow. Using DEM simulations and continuum modeling to examine other protocols with varying dynamical behaviors in Sec. IV, we observe sensitive segregation pattern formation in response to weak perturbation of the flowing layer. We discuss our finding and present our conclusions in Sec. V.

II. NONMIXING STRUCTURES AND SEGREGATION

The system we study is a half-filled $R_o = 7$ cm radius spherical tumbler with an initially uniform size-bidisperse mixture of noncohesive large (4 mm, blue) and small (2 mm, red) diameter spherical particles. The tumbler is repeatedly rotated about orthogonal axes by angles θ_z followed by θ_x, a protocol of (θ_z, θ_x). For each rotation, the granular bed is first rotated from horizontal to its repose angle, then rotated by the specified angle, then rotated back to horizontal. Segregation patterns are typically visible after three to six protocol iterations and fully developed after $N = 15$–20 iterations in both experiments [32] and in our DEM simulations; see, e.g., Video S.1 in the Supplemental Material [34].

Although segregation patterns are reported in previous experiments [32], it is difficult to fully understand how these patterns form from visualizing the accumulation of particles at the clear wall of the tumbler alone. Here we use DEM simulations to examine the flow and segregation as it develops (see Appendix C for DEM simulation details). To validate the DEM simulations, segregation patterns for the $(57^\circ, 57^\circ)$ protocol are compared to experimental results [32] for three distinct large-particle mixture fractions, $f = \{0.05, 0.15, 0.25\}$; see Fig. 2. The tumbler rotation speed, ω, is 3 rpm in the simulations and 2.6 rpm in the experiments. The associated Froude number, $\mathrm{Fr} = R\omega^2/g \approx 6 \times 10^{-4}$, is at the lower end of the rolling/cascading regime in tumbler flow, resulting in a thin continuously flowing particle layer at the flat free surface [6,35]. The DEM simulation is rendered from below using POV-Ray [36] to match the experimental images. The segregation patterns for all three large-particle fractions in the DEM simulations reproduce the experiments in that three distinct large-particle regions of similar shape and extent are observed, corresponding to nonmixing regions A1, B2, and B3 in the Poincaré section; see Fig. 1.

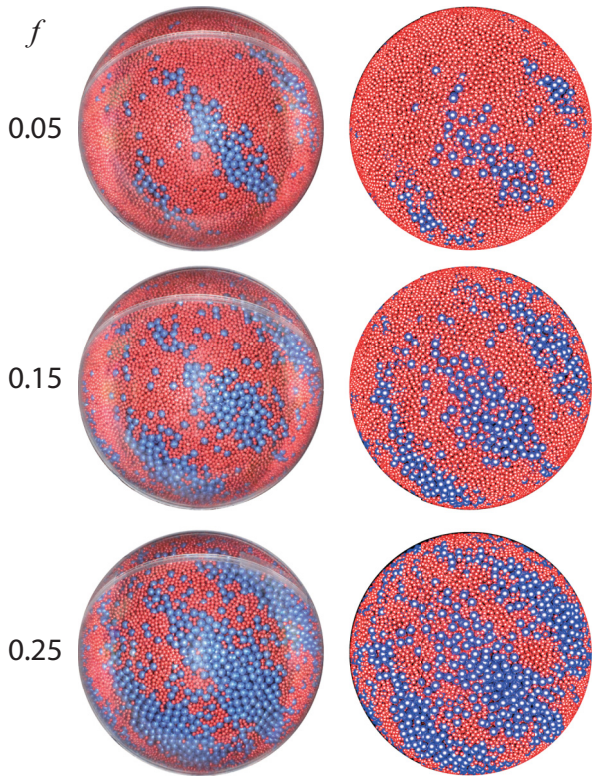

FIG. 2. Comparison of segregation patterns in (left) experiment [32] and (right) DEM simulation at $N = 30$ iterations for the $(57^\circ, 57^\circ)$ protocol using mixtures of 4 mm blue (shaded gray) and 2 mm red (gray) particles in a half-filled spherical tumbler of radius $R_o = 7$ cm for three large-particle fractions f (rows) viewed from below.

A. Large-particle motion in nonmixing regions

We use the DEM simulations to analyze the motion of large particles in the nonmixing islands, shown in Fig. 1, after the segregation pattern reaches steady state. For the $(57^\circ, 57^\circ)$ protocol considered in detail here, each island returns to the same position after three iterations of the protocol (the periodicity of the nonmixing structure depends on the protocol [24,27–29,32,37]). Thus, in Figs. 1(a) and 1(b), A1 moves to the position of A2 after one iteration, to the position of A3 after two iterations, and returns to its original position after three iterations [25,29]. The flow of large particles in the nonmixing islands as they cross the free surface is shown in Fig. 3 (see also Video S.1 in the Supplemental Material [34]). To aid visualization, the tumbler orientation in the figure is offset by the free-surface angle, and small particles are not rendered. Large particles associated with island A3 are colored gold and the surrounding region is highlighted in yellow, while large particles not in A3 are colored blue. The free surface flow direction is indicated by the arrow.

In steady state, as shown in Fig. 3, large particles are concentrated in the six nonmixing regions. During the z-axis rotation (left column), A3 rotates up from the solid-body region (bulk) into the flowing layer. At $2/3$ of the z-axis rotation (third row), A3 is stretched as it transits the free surface on one side of the flowing layer. Simultaneously, but not highlighted, nonmixing region B1 on the other side of the free surface is

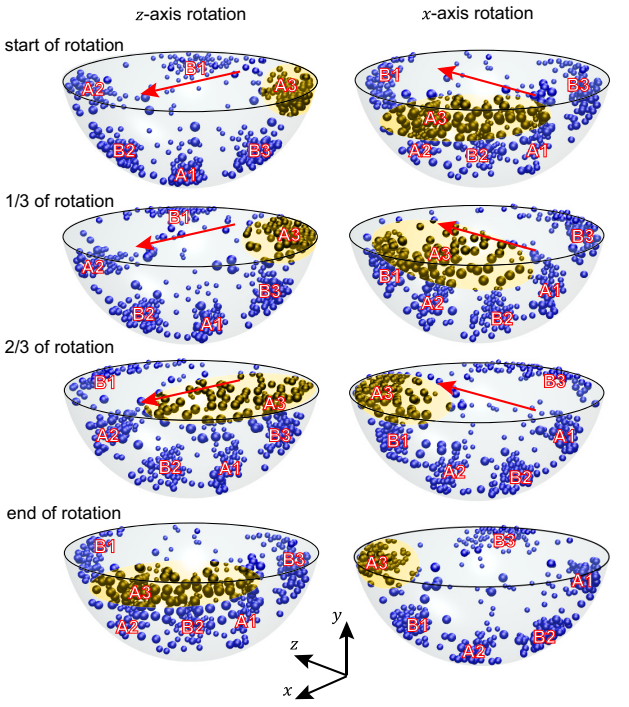

FIG. 3. Large-particle movement in a DEM simulation during the $N = 31$ iteration of the (57°, 57°) protocol for an initially uniform mixture with large-particle fraction $f = 0.05$. The free surface corresponds to the flat portion of the hemisphere, which is offset from the repose angle to horizontal for ease of visualization. Arrows indicate streamwise velocity in the flowing layer. Labels identify two groups of nonmixing clusters A1–A3 and B1–B3.

also stretched as it flows down the free surface. The other four islands remain in the bed of nonflowing particles and rotate as a solid-body with the tumbler. At the end of the z-axis rotation, both A3 and B1 land on the downstream end of the flowing layer after crossing the z-axis. In the subsequent x-axis rotation, B1 is buried in the bulk near the tumbler wall and undergoes solid-body rotation, while A3 reenters the flowing layer. At $1/3$ of the x-axis rotation, region A3 again spreads across one side of the flowing layer, but then contracts again at $2/3$ rotation as it reenters the bed of nonflowing particles. Region B3 also flows down the surface during this portion of the iteration. After this biaxial iteration, region A3 lands on the far left corner of the surface where A2 had started at the beginning of this iteration. The motion of A3 differs during the two rotations that define the protocol. A3 stretches the most in the last $2/3$ of the first rotation (θ_z) and in the first $2/3$ of the second rotation (θ_x) because it is closer to the free surface at the end of the first rotation than at the start. Regions A1, A2, and B2 do not enter the flowing layer during this iteration, but they do so during subsequent iterations. With two additional iterations of the protocol, all nonmixing regions pass through the flowing layer twice and return to their starting positions, thereby leading to the period-3 pattern evident at the tumbler wall.

Finally, we note that the continuum model shows that only the center of each nonmixing region is strictly periodic—the rest of the island rotates about this fixed point of the Poincaré section by an amount determined by the protocol and the particle fill level [37]. Similar rotation of the particle clusters is also evident in the DEM simulations and experiments, but it is less pronounced due to the simultaneous action of collision-driven particle diffusion.

B. Large-particle spatial distribution

The average local large-particle concentration, c_L, near the free surface in steady state ($N \gtrapprox 13$) from DEM simulation is compared to the CM-predicted locations of the nonmixing regions for three different large-particle mixture fractions, f, in order to quantify the spatial distribution of large particles. The large-particle concentration is measured by projecting the position of all large particles in a hemispherical shell of thickness $0.9 < r < 1$ onto a 2D plane using a Lambert azimuthal projection [38] with an equal area grid [28,39], as shown in Fig. 4. The six dark elliptical regions indicate the high c_L values associated with nonmixing islands for the three values of f. The boundaries of nonmixing islands predicted by the CM [red (gray) curves] are projected to the 2D plane in the same manner. For $f = 0.05$, most large particles occupy the nonmixing regions predicted by the CM. At $f = 0.15$, the high concentration regions increase in size but remain elliptical. At $f = 0.25$, the high concentration regions remain centered on the CM-predicted nonmixing regions, but large particles also cover the rest of the domain at lower concentrations.

We can also examine particle distributions and 3D structure in a plane through the particle bed that intersects nonmixing regions A1 and B1 in Fig. 5. The majority of large particles in the DEM simulations fall within the KAM tube boundaries (dotted curves), but they are preferentially located near the tumbler wall, i.e., at larger radii. This is readily explained by size segregation. Large particles tend to rise to the free surface when they cascade down the flowing layer and end up near the tumbler wall (large radii), while small particles tend to drop out of the flowing layer before they reach the downstream tumbler wall (at smaller radii). As the large-particle fraction is increased from 0.05 to 0.25, nonmixing regions become more densely packed with large particles, but only to a depth of three to four particle diameters from the tumbler wall, and the high c_L region expands along the tumbler wall. Because the tendency for large particles to accumulate inside nonmixing regions competes with their tendency to segregate to the top of the flowing layer and then deposit near the tumbler wall, large particles eventually accumulate near the tumbler wall but outside the nonmixing regions for $f > 0.05$. At $f = 0.5$ (not shown), the entire surface is covered by large particles and, consequently, segregation patterns are not visible on the tumbler wall.

C. Particle persistence in nonmixing regions

Having confirmed that the DEM simulations reproduce the segregation patterns observed in experiments and characterized their steady-state concentration fields for different large-particle fractions, we now quantify the tendency for particles to remain within nonmixing islands. The concentration patterns shown in Fig. 4 are time averages from the DEM simulations; individual large particles continue to enter and leave the nonmixing regions during the steady-state averaging

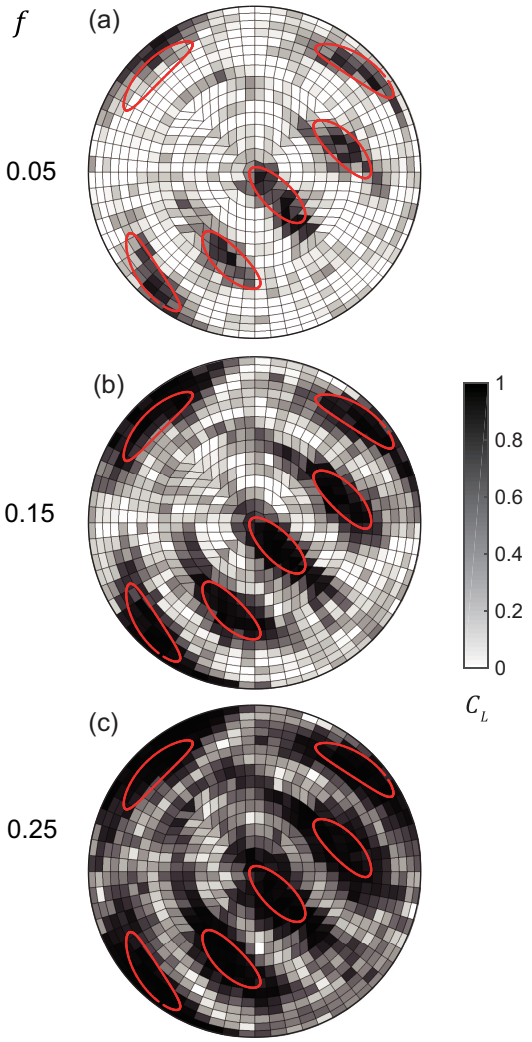

FIG. 4. Local large-particle concentration, c_L, from DEM simulations in steady state averaged over iterations $25 \leqslant N \leqslant 35$ and tumbler radius $(0.9 < r < 1)$ under the protocol $(57^\circ, 57^\circ)$ for increasing (top to bottom) large-particle fraction f as indicated. Concentration fields are visualized from below using a Lambert azimuthal projection, which preserves the area between the 3D hemisphere and the 2D plane. Boundaries of nonmixing islands predicted by the CM at $r = 0.95$ are indicated by red (gray) curves.

interval. To characterize particle movement in steady state, we measure the angular particle displacement field, $\Delta\psi < \pi$, between initial and final positions at integer multiples of the island periodicity, namely three iterations of the protocol for period-3 islands. $\Delta\psi$ is spatially averaged using the equal area grids of the Lambert projection for particles with $0.8 \leqslant r \leqslant 1$ and for two periods (six iterations) in Fig. 6 and six periods (18 iterations) in Fig. 7 for $13 \leqslant N \leqslant 35$ (steady state) and various f. In both figures, $\Delta\psi$ values are shown for large particles (top row) and small particles (bottom row). Note that $f = 0$ and 1 represent monodisperse systems with only small or large particles, respectively, and thus no plots are shown for the zero concentration species.

Over the two flow periods shown in Fig. 6, six distinct regions of small $\Delta\psi$ (dark areas) are apparent for both large and small particles. (Note that gray bins for $f = \{0.05, 0.15\}$ indicate regions with no large particles due to the low f values and the strongly localized segregation.) These regions correlate with nonmixing regions in the CM and indicate that particles tend to remain in the vicinity of their local nonmixing region after six protocol iterations (corresponding to four passes through the flowing layer for particles in KAM regions). The two groups of period-3 regions (A and B) differ only in that they are mirror images of each other one-half iteration apart. They have the same periodicity and, consequently, the same net angular displacement.

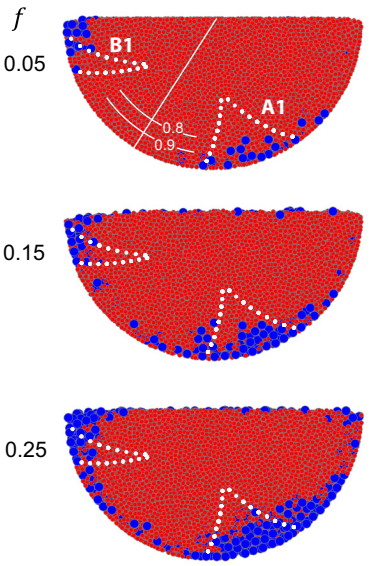

FIG. 5. Steady-state ($N = 30$) particle distributions from DEM simulations for three large-particle fractions f in the intersecting plane indicated by the dashed white line in Fig. 1(b) under the $(57^\circ, 57^\circ)$ protocol. Dotted white curves indicate boundaries of the conelike nonmixing regions (KAM tubes) predicted by the CM. Solid curves indicate radii r.

The variations in the details of the displacement patterns with f are associated with the mixture dynamics. In size-bidisperse cases ($f = \{0.05, 0.15, 0.25\}$), regions of small $\Delta\psi$ for large particles are similar in size despite increasing numbers of large particles. At the highest f shown ($f = 0.25$), large particles tend to stay close to the tumbler wall but cannot all accumulate in the small angular displacement regions due to radial segregation. Consequently, large particles outside nonmixing regions are dispersed into the rest of the domain leading to higher concentrations away from the low displacement regions [Fig. 4(c)]. Small particles exhibit similarly small displacements in nonmixing islands and their vicinity, but they are not visible in Fig. 2 because large particles are predominant at the tumbler wall. Thus, both small and large particles tend to stay in the period-3 nonmixing regions over two periods. Even in the two monodisperse cases ($f = \{0, 1\}$), similar periodic dynamics are observed, but the low $\Delta\psi$ pattern is more localized for $f = 0$ than it is for $f = 1$. This is likely due to the weaker collisional diffusion of small particles, which scales with the square of the particle diameter [40–42].

It is evident that low $\Delta\psi$ regions differ slightly in shape and location for small and large particles in size-bidisperse

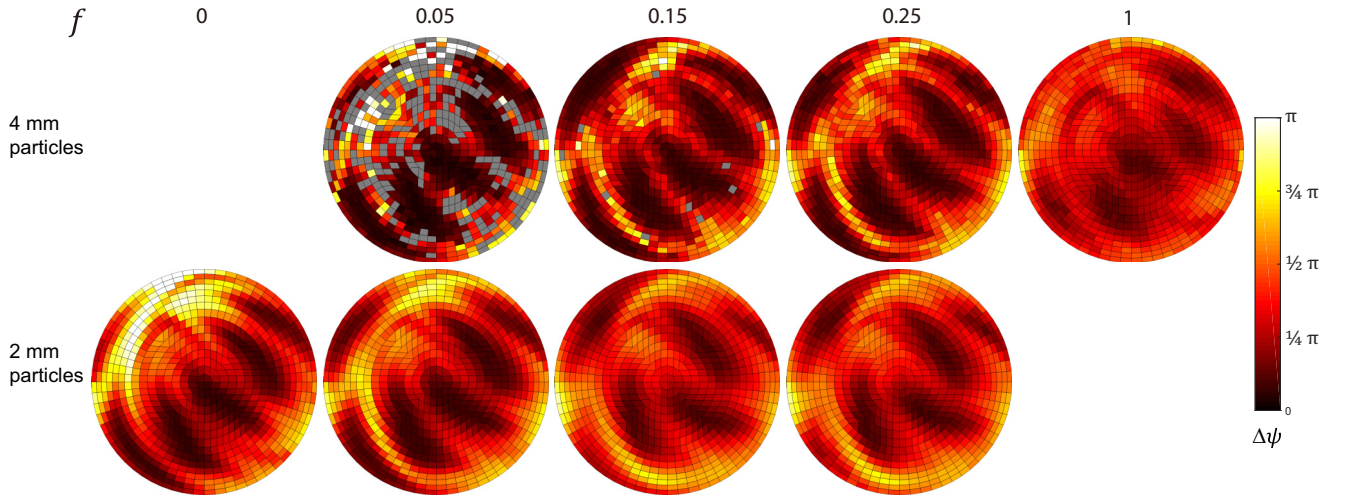

FIG. 6. Net angular displacement, $\Delta\psi$, of large particles (top row) and small particles (bottom row) from DEM simulations with $0.8 \leqslant r \leqslant 1$ over two flow periods (six iterations) during steady-state iterations ($13 \leqslant N \leqslant 35$) of protocol (57°, 57°) for mixtures with large-particle fraction f varied from 0 to 1 as indicated. Grid cells with no large particles are shaded gray. Results are shown in bottom views of the spherical tumbler presented in Lambert azimuthal projections.

cases. For example, the central low displacement region for large particles is closer to the center of the projection than for small particles. This small shift is likely a consequence of the slight difference in the flow of the two particle species in the flowing layer (i.e., small particles reenter the bulk before large particles). Similar differences between low $\Delta\psi$ regions for the bidisperse cases compared to the monodisperse case are also likely a result of slight differences in the flow between the two cases.

While Fig. 6 indicates that the periodic dynamics of particles in nonmixing regions are robust across various mixtures over two periods (six iterations), the displacement over larger numbers of iterations is also of interest. Plots of $\Delta\psi$ over six flow periods (18 iterations) are shown in Fig. 7 for the same simulations. For large particles, a similar pattern of six low $\Delta\psi$ regions is observed compared to Fig. 6 at all f, but with larger values of $\Delta\psi$ due to the greater influence of collisional diffusion and chaotic mixing over more iterations in Fig. 7. $\Delta\psi$ increases with increasing f, and the low displacement regions are faint at $f = 1$. This is likely due to the increasing fraction of large particles outside of the KAM tube at the same projected location as f is increased; see, e.g., Fig. 5. For example, at $f = 1$ a much larger percentage of large particles are outside the KAM tube than at $f = 0.05$, where nearly all large particles are at the tumbler wall and inside the KAM tube. For small particles, the low $\Delta\psi$ regions also fade with increasing f, and they are no longer apparent for $f \geqslant 0.15$. This is likely due to two causes. First, with increasing f, small particles are

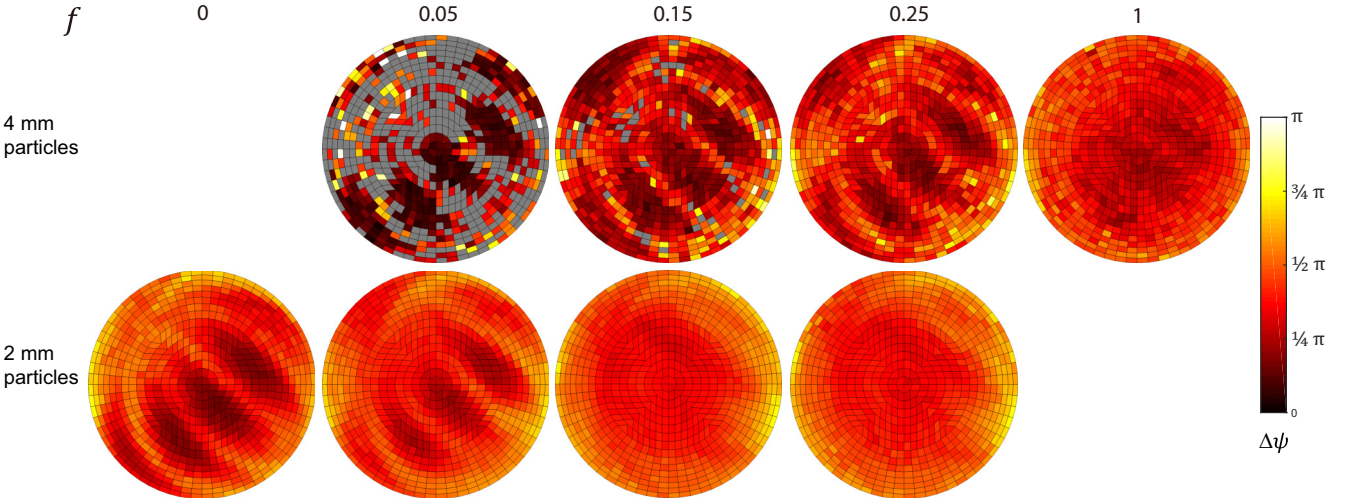

FIG. 7. Net angular displacement, $\Delta\psi$, of large particles (top row) and small particles (bottom row) from DEM simulations with $0.8 \leqslant r \leqslant 1$ over six flow periods (18 iterations) during steady-state iterations ($13 \leqslant N \leqslant 35$) of protocol (57°, 57°) for mixtures with large-particle fraction f between 0 and 1. Grid cells with no large particle are gray. Results are shown in bottom views of the spherical tumbler presented in Lambert azimuthal projections.

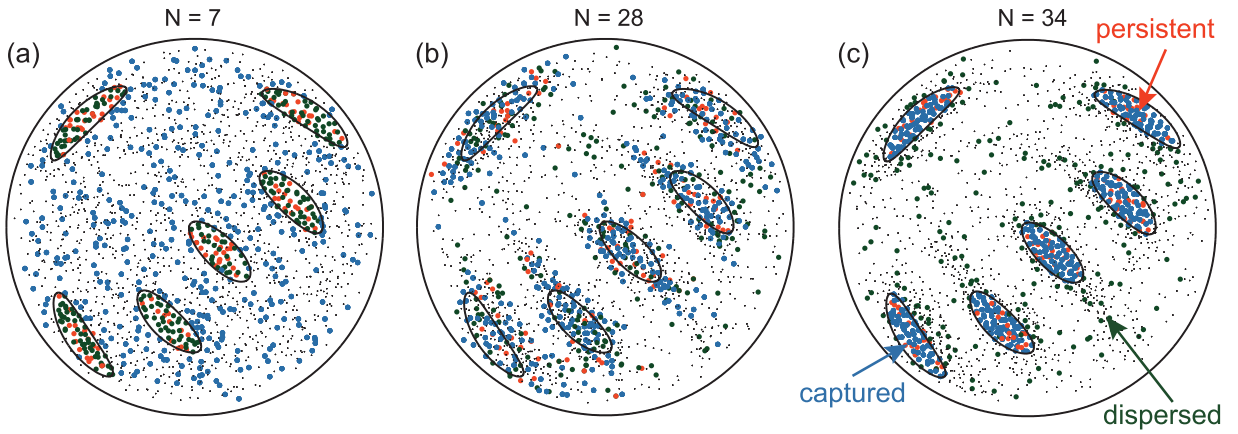

FIG. 8. Development of surface segregation patterns as shown by tracking large particles through barriers to mixing over $7 \leqslant N \leqslant 34$ iterations of (57°, 57°) protocol in DEM simulations viewed from below. "Persistent" particles [orange (light gray)] start and end in nonmixing regions, "captured" particles [blue (gray)] start in the chaotic region and end in nonmixing regions, and "dispersed" particles [green (dark gray)] start in nonmixing regions and end in the chaotic region. All other large particles start and end in the chaotic region (small black dots). Transport barriers (closed black curves) are determined from the CM.

displaced by large particles further from the wall to smaller radii where the nonmixing region (KAM tube) narrows [Fig. 1(b)]. Thus, compared to $f = 0$ where small particles are against the tumbler wall, fewer small particles follow the periodic movement of the nonmixing region at higher f. Second, small particles in the three to four large-particle-thick region of the KAM tube near the tumbler wall are in close proximity to large-particle enriched regions where the collisional diffusion is higher than in pure small-particle regions.

The DEM simulation results in this section demonstrate that flow in the spherical tumbler under the (57°, 57°) protocol produces periodic behavior independently of whether the mixture is monodisperse or bidisperse. This confirms that the underlying spatial and temporal structure of the segregation patterns is inherent to the tumbler dynamics. The DEM simulation results also show that large particles concentrate inside nonmixing regions predicted by the continuum model and remain there over multiple periods. However, why large particles accumulate in the nonmixing regions of the CM remains to be explained.

III. MECHANISM FOR SEGREGATION PATTERN FORMATION

Our previous paper describing segregation patterns in experiments [32], e.g., those in Fig. 2, suggests that the spatial overlap between large-particle-rich regions in experiments and the nonmixing regions in the continuum model is related to the enhanced tendency of large particles to remain in nonmixing regions. This is confirmed by the angular displacement plots in Figs. 6 and 7, which show that the mobility of large particles in nonmixing regions is reduced compared to monodisperse cases, where transport across the mixing barriers is mostly due to collisional diffusion. The remaining question, then, is what drives large particles to preferentially cross transport barriers into nonmixing regions? While the motion of the large-particle clusters is evident in Fig. 3, it does not explain the mechanism that creates them.

A. Pattern evolution in DEM

To determine how large particles accumulate in nonmixing regions, we first use DEM simulation data to track large particles from when they initially segregate radially to the free surface and are relatively uniformly distributed across the surface ($N \approx 7$) until $N = 34$, which is well after the steady-state segregation pattern has developed. Figure 8 plots the positions of four large-particle groups comprising the entire population of 1980 large particles in the DEM simulation: "persistent" large particles that start and end in the same CM-predicted nonmixing region [orange (light gray), 124 particles]; "captured" large particles that are initially outside nonmixing regions at $N = 7$ but are inside at $N = 34$ [blue (gray), 429 particles]; "dispersed" large particles that start inside nonmixing regions but end outside those regions [green (dark gray), 241 particles]; and all other large particles (small black dots, 1186 particles). Small particles are not shown. As the segregation pattern starts to form ($N = 7$), large particles are distributed throughout the tumbler with 365 particles [orange (light gray) and green (dark gray)] in the nonmixing regions. At $N = 28$, the density of blue (gray) large particles is noticeably increased in and around the nonmixing regions. Additionally, some of the persistent particles [orange (light gray)] are outside but still in the immediate vicinity of the nonmixing regions. At $N = 34$, large particles are densely clustered in the nonmixing regions [544 orange (light gray) and blue (gray) particles, many overlaying one another in the figure] and most of the other large particles [green (dark gray) and small black dots] closely surround the nonmixing regions. Clearly, many large particles have crossed transport barriers predicted by the CM to accumulate in these nonmixing regions.

B. Modified continuum model

The accumulation of large particles in nonmixing regions in experiments and in DEM simulations described above clearly indicates that large particles do not exactly follow the

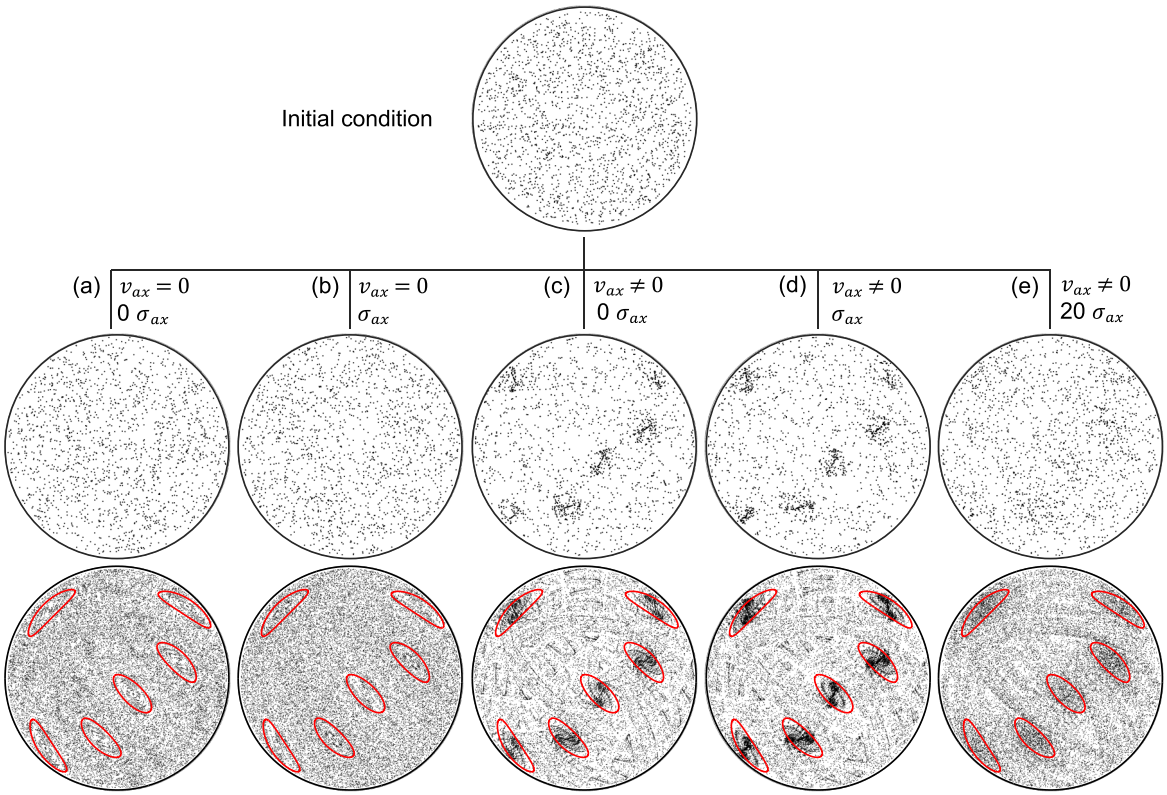

FIG. 9. Continuum model (CM, $v_{ax} = 0$, $\sigma_{ax} = 0$) and modified continuum model (MCM) results for $(57^\circ, 57^\circ)$ protocol in Lambert azimuthal projection viewed from below: (a) without axial drift or diffusion (CM); (b) with random-walk diffusion of σ_{ax} only; (c) with axial velocity but no diffusion; (d) with axial velocity and diffusion σ_{ax}; (e) with axial velocity and increased diffusion $20\sigma_{ax}$. Top row: Initial random distribution of tracer points. Middle row: Tracer point distribution at $N = 30$ with obvious clustering in (c), (d). Bottom row: Cumulative tracer point positions for $30 \leqslant N \leqslant 45$ and nonmixing island perimeters [red (gray) curves] determined by the CM, which does not include drift or diffusion. Only tracer points in the bulk are plotted.

base flow of the CM. To explain this deviation, we note that previous experiments and simulations have reported a weak axial component of the velocity field in spherical tumbler flows which occurs in the surface flow. This flow results in slow axial drift of particles toward the poles at the flowing layer surface and toward the equator in the deeper portions of the flowing layer [33,43]. As we show below using a modified version of the continuum model, weak axial drift, when combined with radial segregation that keeps large particles near the free surface, is sufficient to explain the segregation patterns we observe. The basic mechanism is as follows. If a large particle enters the flowing layer outside but in the vicinity of a nonmixing region, axial drift will move the large particle closer and potentially into the nonmixing region. Since large particles above a layer of small particles will not sink due to radial segregation, the large particles do not recirculate back toward the equator in the lower portion of the flowing layer as they do for size-monodisperse mixtures, but instead remain near the surface and in the nonmixing island. In steady state, the axial flux of incoming large particles is either balanced by the diffusive flux of large particles out of the island or limited by the presence of large particles already filling the island (e.g., see Fig. 2).

To support the hypothesis that axial drift is sufficient to drive surface segregation pattern formation, the CM is modified by adding an axial drift velocity component to the velocity field of the flowing layer. The axial drift velocity, which varies across the flowing layer, is the measured mean local axial velocity of large particles at the free surface in the DEM simulations before the surface pattern reaches steady state; see Appendix A. (We note that, to the best of our knowledge, it is not possible to calculate the drift velocity from first principles.) In addition, to account for particle collisions, an effective collisional diffusion is also included in the model using a random-walk-like approach in which integer multiples of the standard deviation σ_{ax} of the measured axial velocity are, with equal probability, added to or subtracted from the mean axial velocity at each time step (see Appendix A for details). The resulting modified continuum model (MCM) implicitly includes radial segregation of the large particles as the axial velocity is based on the large-particle motion at the free surface only, matching the steady-state position of radially segregated large particles in the flow.

Comparisons of tracer particle distributions from the CM and the MCM for various parameter values for the $(57^\circ, 57^\circ)$ protocol shown in Fig. 9 demonstrate how axial drift and collisional diffusion affect the accumulation of particles in nonmixing regions. The initial condition (top row) consists of 2000 tracer points (approximating the 1980 large particles used in the corresponding DEM simulations at $f = 0.15$) randomly distributed on a hemispherical shell of radius $r = 0.95$ (approximately one large-particle diameter from the tumbler

wall). The advection scheme used in the MCM ensures that the tracer points stay on this hemispherical shell so that they represent large particles close to the tumbler wall due to radial segregation. Distributions of tracer points (in the bulk only) at $N = 30$ are shown in the middle row of Fig. 9, and cumulative tracer point positions ($30 \leqslant N \leqslant 45$) at each flow period (three iterations) are shown in the bottom row along with red (gray) closed curves corresponding to the perimeters of the nonmixing islands from the CM (i.e., no axial velocity and no diffusion).

Results from the continuum model and the modified continuum model for various parameter values demonstrate how axial drift can drive the accumulation of large particles in nonmixing regions. The CM, without axial velocity or diffusion, and the MCM incorporating only a random-walk diffusion of σ_{ax} do not result in an accumulation of tracer points in the nonmixing regions; see Figs. 9(a) and 9(b). However, when axial drift is present (MCM), tracer points accumulate in nonmixing regions both without diffusion [Fig. 9(c)] and with diffusion of σ_{ax} [Fig. 9(d)]. If the diffusion is too large, though, it overwhelms the axial drift effect so there is little accumulation of large particles in nonmixing regions [see, e.g., Fig. 9(e)].

We further note that the competition between axial drift and collisional diffusion can be characterized by the dimensionless Péclet number, $\mathrm{Pe} = Lu/D$, where L is a characteristic length scale, u is a characteristic velocity scale, and D is the diffusion coefficient. In the context of the MCM used here, we define $\mathrm{Pe} = L_{\mathrm{island}}\langle|v_{ax}|\rangle/[(\alpha\sigma_{ax})^2\Delta t]$, where $\langle|v_{ax}|\rangle$ is the spatial mean of the absolute value of the axial drift velocity, α is a dimensionless constant (e.g., $\alpha \in \{0, 1, 20\}$ in Fig. 9), L_{island} is the characteristic size of an island, and Δt is the integrator time step from the MCM computations [44]. Diffusion overwhelms axial drift in Fig. 9 for $\alpha = 20$, which corresponds to a small value of $\mathrm{Pe} = 0.4$ as expected. Similarly, axial drift is stronger than diffusion for $\alpha = 1$, which corresponds to a larger value of $\mathrm{Pe} = 150$. It is not currently possible to determine either v_{ax} or D (equivalently, σ_{ax}) from first principles, although D can be estimated if the velocity field is known [42].

In this section, we have used the MCM, which is, to a degree, ad hoc (e.g., it assumes large particles are radially segregated and ignores their interactions with each other), to clearly demonstrate that axial drift alone results in large particles being transported across nominal mixing barriers to accumulate in the nonmixing regions of the CM. Moreover, the accumulation of tracer points in the nonmixing islands observed under the MCM with axial drift is only disrupted by diffusion when it is relatively large (i.e., here, $20\sigma_{ax}$ corresponding to a small value of $\mathrm{Pe} = 0.4$), as expected. This result is consistent with observations of large collisional diffusion and the disappearance of segregation patterns in biaxial tumbler systems with small particle size ratios where radial segregation is weak [32].

IV. SEGREGATION PATTERNS FOR OTHER PROTOCOLS

We have examined segregation under the $(57°, 57°)$ protocol to this point, but segregation patterns and barriers to mixing appear in the biaxial spherical tumbler for other protocols [32]. Furthermore, there are protocols and conditions for which segregation patterns do not appear. In this section, we use DEM simulations and the MCM to examine these situations.

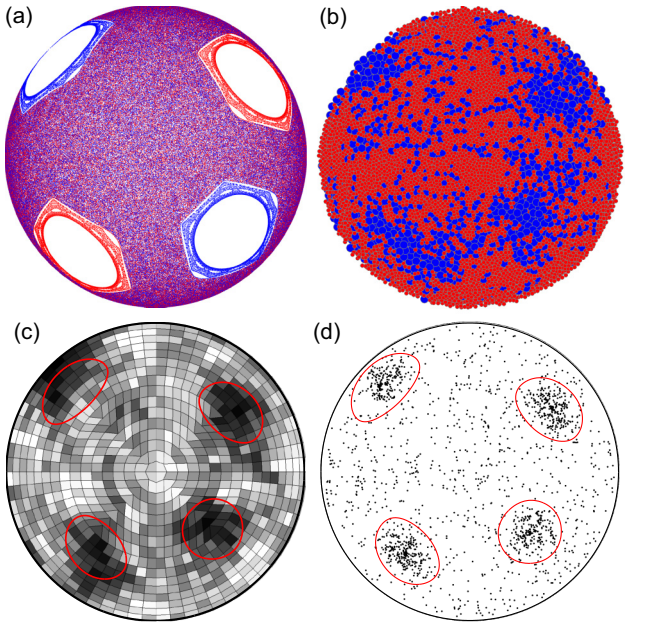

FIG. 10. Segregation pattern under the $(90°, 90°)$ protocol. (a) Poincaré section from CM at $r = 0.95$. (b) Lambert projection of particles ($0.9 \leqslant r \leqslant 1$) in the DEM simulation of a half-filled spherical tumbler with a mixture of $f = 0.15$ large particles at $N = 30$ of the same protocol. (c) Average concentration of large particles ($0.9 \leqslant r \leqslant 1$) in the DEM simulation for $15 < N < 30$ (color map as in Fig. 4). (d) MCM with axial velocity and diffusion σ_{ax} for an initial random distribution of tracer points at $N = 30$. Boundaries of nonmixing islands predicted by the CM are indicated by red (gray) curves in [(c),(d)]. All results are viewed from below.

A. A similar biaxial protocol

There are many other protocols that produce large nonmixing regions that vary in size, location, and periodicity from those generated by the $(57°, 57°)$ protocol [27]. For example, the CM under the $(90°, 90°)$ protocol results in four large period-2 nonmixing regions, as Fig. 10(a) shows, that also act as attractors for large-particle segregation in experiments [32]. In DEM simulations for the same conditions, large particles accumulate in these nonmixing regions [Fig. 10(b)] matching experimental results, and their concentration near the tumbler wall ($0.9 \leqslant r \leqslant 1$) is high (dark regions) in the nonmixing islands predicted by the CM [red (gray) closed curves in Fig. 10(c)].

Applying the MCM to the $(90°, 90°)$ protocol, as in Fig. 9, results in tracer points accumulating in nonmixing regions, as shown in Fig. 10(d). This again indicates that weak axial drift is sufficient to drive the accumulation of tracer points in the nonmixing regions predicted by the CM.

For both the $(57°, 57°)$ and $(90°, 90°)$ protocols, large particles accumulate in the nonmixing islands of the unperturbed CM when the base flow is perturbed by a weak secondary

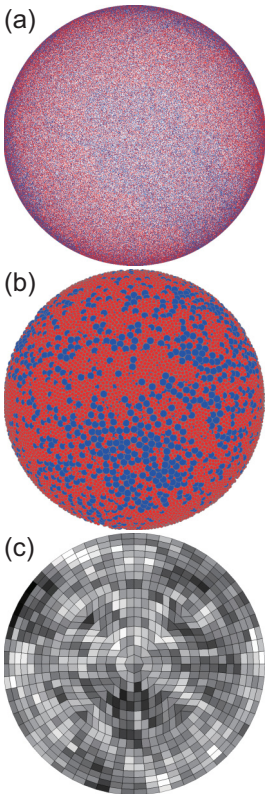

FIG. 11. Absence of segregation patterns for the (68°, 68°) protocol. (a) No nonmixing islands in the Poincaré section of the CM. (b) Bottom view of DEM simulation with initially mixed small red (gray) particles and large blue (dark gray) particles ($f = 0.15$) at $N = 40$. (c) Average concentration in 2D Lambert projection for $26 \leqslant N \leqslant 40$ from DEM simulation data with $0.9 < r < 1$ (color map as in Fig. 4).

flow. Under these conditions, the nonmixing islands of the CM behave instead like sinks [31], allowing large particles to cross the boundaries of the nonmixing islands, which were previously understood as barriers to transport [25,32]. In experiments and DEM simulations, because particles cannot overlap, large particles fill the nonmixing islands and then surround the nonmixing island as f is increased. In steady state, there is a balance between diffusive fluxes, which drive large particles away from the high concentration regions surrounding the islands, and the actions of the perturbed base flow (i.e., axial drift) which drive them into the islands.

B. No segregation-pattern example

So far we have shown that large particles cluster in nonmixing regions as a result of weak axial drift that drives them across the transport barriers of the unperturbed flow. Thus, two elements are necessary for segregation: weak flow perturbations and the existence of nonmixing regions. To further support our understanding of segregation in the BST, we consider a protocol for which no large nonmixing islands exist in the Poincaré section, and therefore one for which we would expect segregated surface patterns to be absent. Specifically, we consider the (68°, 68°) protocol of the CM in Fig. 11(a) for which no apparent nonmixing islands are present in the Poincaré section, which is a very different situation from the large islands present in (57°, 57°) (Fig. 1) and (90°, 90°) (Fig. 10) protocols.

In DEM simulation of the (68°, 68°) protocol with initially mixed large and small particles, the large particles radially segregate to the tumbler wall where they distribute nearly uniformly across the surface [Fig. 11(b)]. Although some weak clustering is evident, the average large-particle concentration is significantly more uniform than in the two previous protocols with large nonmixing regions, i.e., (57°, 57°) and (90°, 90°), and there is no obvious periodic pattern. Furthermore, particles in these weak clusters quickly disperse and do not return to the same groups as occurs for the (57°, 57°) protocol shown in Fig. 3. Similar results with little to no segregation are also observed for (60°, 75°) and (65°, 76°), which also have unstructured Poincaré sections in the CM. Thus, without nonmixing regions, robust segregation patterns do not develop.

C. Global transport barriers

In the previous example of the (68°, 68°) protocol that lacks nonmixing regions, persistent segregation patterns do not occur and large particles spread relatively uniformly across the surface. However, some protocols that lack significant nonmixing regions can still exhibit nonuniform distribution of large particles depending on the initial conditions of the mixture. In particular, we previously identified protocols that lack nonmixing regions but exhibit global mixing barriers between chaotic mixing regions [25]. To understand the effects of global mixing barriers on large-particle distribution in these cases, consider the (45°, 45°) protocol. Similar to other cases, the Poincaré section is generated from the CM by tracking points seeded on the interface between the flowing layer and the bulk at $r = 0.95$ at the start of the first [red (gray)] and second [blue (dark gray)] rotation. The Poincaré section in Fig. 12(a) shows interpenetrating blue (dark gray) and red (gray) dominated fingerlike regions separated by a "leaky" global mixing barrier [25,32]. This structure results from the interactions between the flowing layer and the underlying dynamical system of the biaxial protocol [21,23,25,26], which create invariant ergodic structures that are barriers to mixing [30].

Although thin elongated nonmixing regions (white) exist in the center of each of the six "fingers," they occupy only a relatively small area that does not significantly influence segregation. Instead, the stable [shown in green (light gray)] and unstable manifolds of the CM flow [32] (see Appendix B) are responsible for the observed global mixing barrier that defines the red (gray) and blue (dark gray) dominated regions. That is, the stable and unstable manifolds, which drive chaotic transport in these mixing regions, reside entirely in either of the two domains. This is unlike the cases we examined in Figs. 1(a) and 4(a), where every manifold fills the entire chaotic sea and encloses every nonmixing region, as we have shown previously [32]. In Fig. 12(a), the blue (dark gray) dominated region has two of its three "finger" structures in the bulk, while the third one is mostly in the flowing layer (not visible from the bottom view of the tumbler), with only

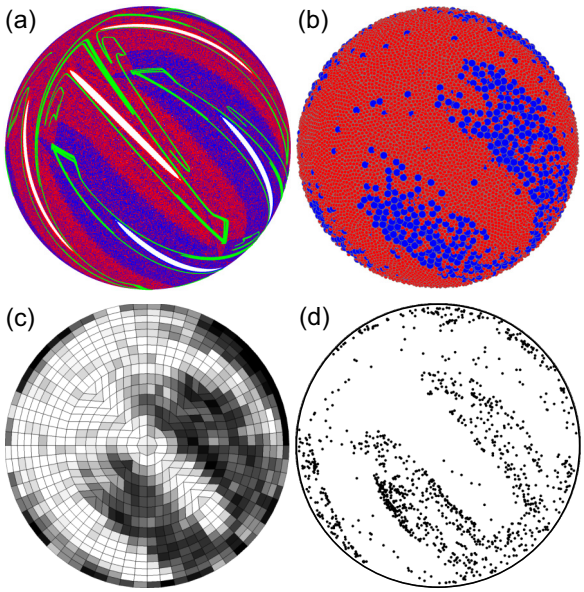

FIG. 12. Global mixing barrier spanning the tumbler for the $(45^\circ, 45^\circ)$ protocol (bottom view). (a) Poincaré section from the CM shows large interpenetrating fingerlike structures. Stable manifolds of the CM flow are indicated by green (light gray) curves. (b) Large blue (dark gray) particles with $f = 0.15$ in DEM simulations remain primarily in the half of the domain in which they are initially placed after $N = 30$ iterations. (c) Average concentration of large particles $(0.9 \leqslant r \leqslant 1)$ in the DEM simulation for $15 \leqslant N \leqslant 30$ (color map as in Fig. 4). (d) Large-particle distribution from the MCM ($v_{ax} \neq 0, \sigma_{ax}$) at $N = 30$ for the same initial conditions as in (b).

its edge extending into the bulk, as is barely visible on the periphery of the image.

Figures 12(b) and 12(c) demonstrate how the global mixing barrier can result in pattern formation for a mixture of large particles and small particles in the DEM simulation when the large particles are initially located in the flowing layer (not the well-mixed initial condition used in the previous examples), which corresponds with the blue (dark gray) finger in the flowing layer of the CM [Fig. 12(a)]. After $N = 30$ iterations, diffusion and chaotic mixing distribute the large particles relatively uniformly on the side of the mixing barrier on which they are initially placed, but very few large particles cross the global mixing barrier into the other half, i.e., the small-particle [(red gray)] dominated region. This behavior stands in contrast to that for both the $(57^\circ, 57^\circ)$ and $(90^\circ, 90^\circ)$ protocols, where large particles concentrate in nonmixing islands by crossing the barrier to mixing that separates the chaotic sea from the periodic regions, and to that for $(68^\circ, 68^\circ)$, where large particles spread uniformly throughout the entire domain.

MCM results for the $(45^\circ, 45^\circ)$ protocol with the same initial conditions as the DEM simulation (i.e., all large particles in the flowing layer) demonstrate that the global mixing barrier persists even in the presence of axial drift and collisional diffusion, as shown in Fig. 12(d). The global mixing barrier is surprisingly persistent in the MCM, even with higher levels of diffusion ($20\sigma_{ax}$, not shown). Two reasons may explain this persistence. First, the global mixing barrier in this example separates two chaotic regions, while the barriers to mixing in previous examples, i.e., $(57^\circ, 57^\circ)$ and $(90^\circ, 90^\circ)$, separate nonmixing periodic regions from the chaotic region. Therefore, the global mixing barrier does not bound a sink under the influence of axial velocity as it does for the other two protocols. Second, the axial drift field is predominantly tangent to the boundary between the red (gray) and blue (dark gray) dominated regions when it crosses the flowing layer so that axial transport redistributes large particles along the boundary with a significantly higher frequency than across it.

D. Density-driven segregation

To this point we have described the formation of segregation patterns due to particle size differences. However, bidisperse mixtures of spherical particles varying only in density can also result in radial segregation. Do these density-bidisperse mixtures in the BST system form surface segregation patterns, and if so, are they similar to those for size-driven segregation? To achieve a similar segregation strength to the size-ratio-2 mixture used here, the density ratio $R_\rho = \rho_1/\rho_2$ of the two species needs to be large, $8 < R_\rho < 10$ [45,46]. Two DEM simulations are performed for the $(57^\circ, 57^\circ)$ protocol using equal diameter particles (2 mm) with $R_\rho = 3$ (2 vol. % of $\rho = 2000$ kg m^{-3} and 98 vol. % of $\rho = 6000$ kg m^{-3}) and $R_\rho = 8$ (2 vol. % of $\rho = 1000$ kg m^{-3} and 98 vol. % of $\rho = 8000$ kg m^{-3}; see [47]).

For both density ratios, lighter particles radially segregate to the tumbler wall, similar to larger particles in the size-bidisperse cases. However, only weak segregation patterns occur, as shown by the particle distributions and the average lighter-particle concentration in Fig. 13. For $R_\rho = 3$, the overall surface density is lower than for $R_\rho = 8$, but the segregation pattern is stronger. The weaker segregation patterns for $R_\rho = 8$ appear to be due to the significant degree of bouncing of lighter particles in the flowing layer (i.e., higher lighter-particle diffusion) and the possibly corresponding smaller magnitude of mean axial drift in the flowing layer.

Based on DEM simulations and models (CM and MCM) in this section, there appear to be two requirements on the parameters of the BST for spontaneous pattern formation to occur. These are (i) rotational protocols that produce large nonmixing islands in the CM (e.g., Fig. 10 versus Fig. 11), and (ii) strongly radially segregating mixtures with low collisional diffusion relative to axial drift (e.g., consider Fig. 13, where these conditions are not well met). It is also worth noting that the existence of axial drift alone does not guarantee that transport barriers of the CM will be crossed (e.g., Fig. 12); the barrier must also be nonparallel to the axial drift direction as it passes through the flowing layer.

V. DISCUSSION AND CONCLUSIONS

Segregation patterns in experiments with size-bidisperse granular materials in a 3D tumbler system can be predicted from the corresponding Poincaré sections [25,32]. This is remarkable and also puzzling because Poincaré sections are wholly *kinematic* and depend only on the details of the mixing protocol [23,31], whereas the *dynamics* of segregation is driven by the characteristics of the granular mixture. The apparent ability of Poincaré sections to predict segregated pat-

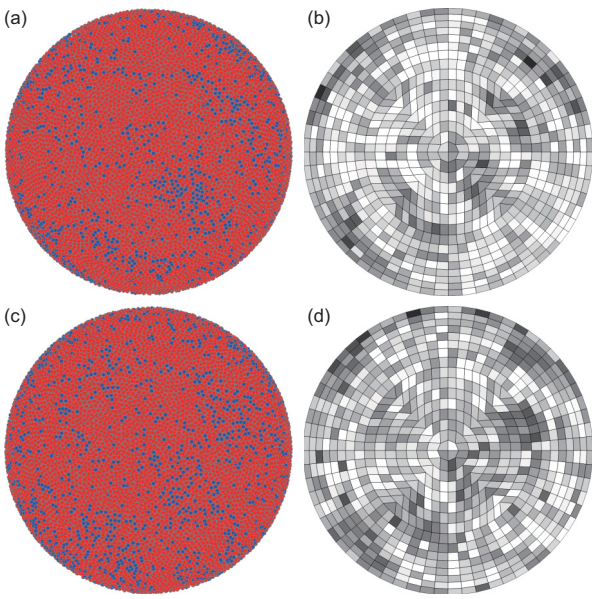

FIG. 13. Segregation of density-bidisperse mixtures of lighter [blue (dark gray)] and heavier [(red gray)] 2-mm-diam particles in DEM simulations for the (57°, 57°) protocol at density ratios (a),(b) $R_\rho = 3$ and (c),(d) $R_\rho = 8$. (a),(c) Bottom view of DEM simulations at $N = 30$, and (b),(d) average concentration of lighter particles for $25 \leqslant N \leqslant 35$ for $0.97 \leqslant r \leqslant 1$ (one-particle-diameter-thick layer adjacent to the tumbler wall) indicates weak pattern formation (color map as in Fig. 4, except for lighter particles).

terns was the genesis for the detailed investigation presented in this paper to uncover how segregation interacts with nonmixing islands in the flow. Details are important in revealing the nature of the interaction, which we summarize here.

It is well understood that when a size-bidisperse mixture is rotated in a tumbler, large particles tend to segregate to the surface of the flowing layer and, consequently, deposit in the bulk near the tumbler wall. However, the mechanism that causes large particles to form the patterns observed on the surface in experiment [32] was unclear. Here we have used DEM simulations and continuum models to gain the following understanding of BST segregation. Before initially well-mixed size-bidisperse particles are tumbled, the probability of finding large and small particles in nonmixing regions and chaotic regions is uniform and proportional to their relative volumes. However, once tumbling commences and radial segregation ensues, large particles rise to the surface of the flowing layer, which has two consequences. First, radial segregation causes the large particles to deposit into the bulk near the tumbler wall, which is where the nonmixing regions (i.e., KAM tubes) predicted by the base flow are the largest [see Fig. 1(b)]. Second, particles on the surface of the flowing layer drift axially into nonmixing islands. Consequently, large particles preferentially accumulate in (due to axial drift) and at the top of (due to radial segregation) the three-dimensional nonmixing regions. At the same time, small particles fall to lower levels of the flowing layer due to radial segregation, and thus tend to reside beneath the large-particle layer visible at the tumbler wall in the bulk. The segregation pattern can only be observed for large-particle concentrations less than about 0.3 for a size ratio of 2. Otherwise, radial segregation causes the entire tumbler wall and flowing layer surface to be fully covered by large particles. Likewise, when nonmixing islands are absent from the base flow, there are no regions for particles to accumulate, and robust segregation patterns are not observed; see, e.g., Fig. 11.

Direct support for this understanding of size-bidisperse mixture segregation in the BST is provided by a modified continuum model, which incorporates the local axial velocity measured from particles in the top layer of the flowing layer in DEM simulations (similar weak axial drift in monodisperse particle flow was previously observed in single-axis rotation of spherical tumblers [33,43,48]). While the continuum model without axial drift predicts [27,28], and experiments in monodisperse flows confirm [25], that the boundaries of nonmixing regions are transport barriers, the modified continuum model not only predicts material transport through the boundaries, but also that these nonmixing regions act as sinks that draw material (specifically large particles at the surface of the flowing layer) into them as observed in experiment [32] and here in our DEM simulations. The axial drift, although quite small compared to the streamwise flow, significantly changes the dynamical system features and is a key component of the segregation pattern formation. It is also important to note that axial drift in the BST cannot currently be determined from first principles (i.e., knowing only the mixture composition and the tumbler diameter, rotation rate, and protocol) because continuum models of the flow dynamics are not yet sufficiently accurate.

We also consider another category of nonmixing behavior, namely the global mixing barrier [25,32]. Instead of separating nonmixing from chaotic regions, global mixing barriers separate distinct chaotic regions. Evidence of particles confined to regions separated by these barriers for a size-bidisperse system in experiment was reported, but not previously understood [32]. Here we observe the same behavior in DEM simulation, and we show using the MCM that the mixing barrier is insensitive to axial drift perturbations of the base flow. We speculate that global mixing barriers are related to invariant ergodic subsets that have only recently been described in the BST system [30].

Although the axial drift mechanism is sufficient to explain the segregation patterns we observed, it is likely that other effects are at play. These include large particles starting at positions midway along the length of the flowing layer after switching rotation axes, differences in how quickly the small and large particles start and stop in the flowing layer at the start and end of a rotation, respectively, variations in how large and small particles are buried in the bulk after they leave the flowing layer, and particle interactions with the curved tumbler wall that can affect segregation patterns [48]. These mechanisms likely act simultaneously with the axial drift mechanism in ways that may also affect the segregation patterns.

The appearance of segregation patterns in biaxial spherical tumbler flow, which is a relatively simple 3D tumbler geometry, suggests that analogous segregation patterns can occur in industrial mixers used in the pharmaceutical, chemical, and agricultural processing industries. In these settings, the goal is usually to avoid segregation and assure mixing, something

that may be critical to the process. In attempts to effectively mix granular components in industry, a variety of tumbler geometries are used, including V-blenders, double-cone blenders [49], and dual-axis cylindrical tumblers [50,51]. However, the results of this study suggest that using a 3D tumbler geometry, even with multiaxis rotation, does not ensure mixing. In fact, the combined effects of the velocity field (which can produce nonmixing regions and transport barriers) and segregation can result in surprising effects that may frustrate attempts at mixing in 3D tumblers.

ACKNOWLEDGMENTS

M.Y. thanks Lauren Smith, Thomas Lynn, and Umberto D'Ortona for valuable discussions, and Ryan Jones for helping to develop the DEM simulation.

APPENDIX A: THE CONTINUUM MODEL AND MODIFICATION WITH AXIAL VELOCITY

In the original continuum model [23,25], particles flow down the surface in a thin flowing layer that lies on top of nonflowing particles in the bulk that move in solid-body rotation with the tumbler. The flow is assumed to be two-dimensional in planes perpendicular to the axis of rotation. The flowing layer velocity is approximated by a constant shear rate velocity profile. For rotation about any axis (the z-axis here with x in the streamwise direction and y normal to the free surface), the nondimensionalized velocity field $\mathbf{u} = (u, v, w)$ is piecewise defined such that the flowing layer ($0 \geqslant y \geqslant -\delta$) velocity is

$$\mathbf{u}_{fl} = ((\delta + y)/\epsilon^2, xy/\delta, 0)$$

and the bulk ($y < -\delta$) solid-body rotation velocity is

$$\mathbf{u}_b = (y, -x, 0).$$

The interface of the lenticular flowing layer with the bulk is located at $\delta(x, z) = \epsilon\sqrt{1 - x^2 - z^2}$, where $\epsilon = \delta(0, 0) = \sqrt{\omega/\dot{\gamma}}$ is the maximal dimensionless flowing layer depth for shear rate $\dot{\gamma}$ and angular rotation velocity ω. All variables are dimensionless—lengths are normalized by the tumbler radius R_o, and the rotation time is normalized by $1/\omega$. Note that we assume the particles gain the velocity described above immediately as the tumbler starts to rotate, and that they stop moving instantaneously as the tumbler stops rotating. This original continuum model, which includes the stretching characteristic of chaotic flows [52], is parametrized by the flowing layer depth ϵ, which is set to 0.15 to match the conditions in the experiments ($\omega = 2.6$ rpm) [25]. The same rotation speed about both the x-axis and the z-axis is assumed, so that $\epsilon_x = \epsilon_z$.

To add axial drift to the CM model, the mean local axial velocity on a grid, $v_{\mathrm{ax}}(i, j)$, is obtained from DEM simulations by averaging the axial velocity of each large particle in the flowing layer on a 30×30 grid covering the flowing layer. Each grid cell is about one large-particle diameter (d_{L}) in both the x and z directions. Large particles that travel for at least half of the rotation action are tracked to exclude those that are only briefly in the flowing layer (i.e., at the beginning or end of the rotation). The tracking sequence starts with any large particle that is within d_{L} of the free surface, noting that large particles readily segregate to near the free surface of the flowing layer. The tracking sequence ends when the particle's streamwise velocity reverses sign, which corresponds to when a particle deposits into the bulk. Axial velocities of particles are recorded in each grid cell every 0.1 s, which corresponds to 1.8° of tumbler rotation at the 3 rpm rotation rate, over the entire tracking sequence (one flowing layer pass consists of about 18–20 axial velocity measurements per large particle in the flowing layer). The axial velocities are sampled over the initial 15 iterations of the simulation before significant surface segregation occurs for eight simulations with $f = 0.15$, and then averaged in each grid cell.

The axial drift of the large particles is zero at the equator and toward the poles on each side of the equator, until near the poles where large particles move away from the poles, since only small particles can sustain contact with the tumbler wall in the thin flowing layer at the poles [48]. The maximum magnitude of the axial drift is about one-half large-particle diameter per pass through the flowing layer, which is somewhat smaller than that found previously [33], likely due to a slower rotation speed and including all large particles in the flowing layer rather than just those visible at the tumbler wall in solid-body rotation.

Note that flow in the MCM is not strictly incompressible because it only tracks large surface particles while neglecting small subsurface particles that migrate axially in the opposite direction. Nevertheless, the MCM allows us to quantitatively illustrate the propensity for large-particle movement under the influence of both the biaxial protocol and weak axial drift. Including the measured axial velocity in the MCM changes the w component of $\mathbf{u}_{\mathrm{fl}}$ from 0 to $w = v_{\mathrm{ax}}(i, j)$, where the indices corresponds to the averaging region at the location of the large particle.

Random-walk diffusion in the axial direction to mimic the effects of collisional diffusion is included by adding or subtracting the standard deviation of the axial velocity in the corresponding grid cell, $\sigma_{\mathrm{ax}}(i, j)$, with equal probability. In MATLAB, this is done using an integer random number generator on the domain [1 2], as $w = v_{\mathrm{ax}}(i, j) + c(-1)^{\mathtt{randi([1,2],1)}}\sigma_{\mathrm{ax}}(i, j)$, where c is a weighting term that adjusts the strength of diffusion. The imposed diffusion is not related to concentration gradient or other possible diffusion mechanisms, such as Taylor dispersion. Although this modified continuum model is simple, it captures the major elements of the flow dynamics, including advection by the streamwise and axial velocities and diffusion.

APPENDIX B: PERIODIC POINTS AND MANIFOLDS OF A DYNAMICAL SYSTEM

The stability of periodic fixed points, their associated manifolds, and the interactions between unstable and stable manifolds largely represent the global dynamics of a smooth system [52]. Periodic fixed points are classified by the eigenvalues of the Jacobian matrix $D\Delta = (\frac{\partial \Delta_i}{\partial x_j})$ for a period-n mapping of $\Delta^n(\boldsymbol{x}) = \boldsymbol{x}$ [23,53]. For the 3D volume-preserving map studied here, the three eigenvalues have a product of $\lambda_1\lambda_2\lambda_3 = 1$. There is a null direction at each periodic point providing a local invariant, corresponding to the eigenvalue of

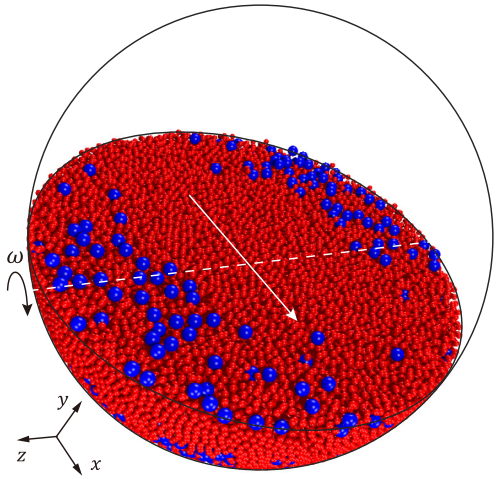

FIG. 14. DEM simulation of a size-bidisperse mixture in a spherical tumbler rotating about the z-axis with angular speed $\omega = 3$ rpm. Particles cross the free surface in a thin flowing layer in the direction indicated by the white arrow and slowly drift toward the poles due to a weak axial velocity (see the main text).

$1, \lambda_1 = 1$ [53]. An elliptic point has two eigenvalues that form a complex conjugate pair with $\lambda_2 = \overline{\lambda_3}$ and $|\lambda_2| = |\lambda_3| = 1$. Therefore, they can be expressed in trigonometric form as $\lambda_{2,3} = \cos\phi \pm i \sin\phi$, where ϕ is related to the internal rotation angle of the elliptic region surrounding the elliptic point. A hyperbolic point has two real eigenvalues, $\lambda_2 = 1/\lambda_3$. Material expands along the direction corresponding to eigenvalue $\lambda > 1$, and it contracts along the direction corresponding to eigenvalue $\lambda < 1$ [54]. The stable manifolds consist of all points that converge to the hyperbolic point as the number of iterations approaches infinity, while the unstable manifolds consist of all points that converge to the hyperbolic point in the reverse time. Therefore, the stable manifolds and unstable manifolds can be traced by tracking points seeded on the corresponding eigenvectors in backward time and forward time, respectively. The unstable manifolds are traced by tracking points seeded on a short line segment of length $0.001R_o$. Positions of tracer points are recorded after every iteration, and the resulting manifolds shown in Fig. 12(a) are trajectories of tracer points advected for 14 iterations. To maintain a uniform density tracing in the presence of fast manifold stretching, new points are back-inserted in intervals between consecutive points that are 5×10^{-5} R_o apart or more after each iteration.

APPENDIX C: DEM SIMULATION

Flows in the biaxial spherical tumbler are simulated using the discrete element method (DEM) with frictional smooth boundaries. Particles are modeled as rigid spheres, and their collisions cause a slight overlap. Contact forces are computed based on the relative overlap and velocity between contacting particles. Thorough discussions of DEM simulations in dense granular flows can be found in the literature, e.g., [55–58], and further details of the methods used here are also described elsewhere [45,46,59]. In brief, a linear-spring dashpot force model is used for normal contacts between two particles: $\mathbf{F}^{\mathrm{n}}_{ij} = [k_{\mathrm{n}}\zeta - 2\gamma_{\mathrm{n}} m_{\mathrm{eff}}(\mathbf{V}_{ij} \cdot \hat{\mathbf{r}}_{ij})]\hat{\mathbf{r}}_{ij}$, where ζ and $\mathbf{V}_{ij}$ represent the overlap and relative velocity, respectively, between two contacting particles i and j. The unit normal vector is denoted by $\mathbf{r}_{ij}$, and the reduced mass is $m_{\mathrm{eff}} = m_i m_j/(m_i + m_j)$. The normal stiffness k_{n} and damping γ_{n} of the granular material are determined from the restitution coefficient e and collision time t_{c} by $k_{\mathrm{n}} = [(\pi/t_{\mathrm{c}})^2 + \gamma_{\mathrm{n}}^2]m_{\mathrm{eff}}$ and $\gamma_{\mathrm{n}} = -\ln(e)/t_{\mathrm{c}}$. Tangential contact forces are modeled using a hybrid Coulomb-like friction approach that models static friction with a spring and sliding friction in the standard way: $\mathbf{F}^{\mathrm{t}}_{ij} = \min(|k_{\mathrm{t}}\beta_{ij} + 2\gamma_{\mathrm{t}} m_{\mathrm{eff}}(\mathbf{V}_{ij} \times \hat{\mathbf{r}}_{ij})|, \mu|\mathbf{F}^{\mathrm{n}}_{ij}|)\mathrm{sgn}(\beta)\hat{\mathbf{s}}_{ij}$, where the tangential stiffness is $k_{\mathrm{t}} = \frac{2}{7}k_{\mathrm{n}}$. The tangential displacement β_{ij} is defined as $\beta_{ij} = \int_{t_{\mathrm{s}}}^{t} \mathbf{V}_{ij} \times \hat{\mathbf{r}}_{ij} dt$, where t_{s} is the initial contact time. The restitution coefficient e is set to 0.87, and friction coefficients μ are 0.6 for particle-particle and particle-wall contacts. In all cases unless specifically noted, the spherical tumbler of radius $R_o = 7$ cm is half-filled with a size-bidisperse mixture of $d = 4$ and 2 mm particles of density $\rho = 2500$ kg m^{-3}. The fractional volume of large particles, f, relative to the total particle volume is varied from 0 to 1. The spherical tumbler is rotated at 3 rpm, which is close to the value of 2.6 rpm in corresponding experiments [25,32]. A rendering of a DEM simulation in the spherical tumbler with a size-bidisperse mixture is shown in Fig. 14.

[1] H. M. Jaeger, S. R. Nagel, and R. P. Behringer, Granular solids, liquids, and gases, Rev. Mod. Phys. **68**, 1259 (1996).
[2] J. Duran, *Sands, Powders, and Grains* (Springer, New York, 2000).
[3] J. M. N. T. Gray, Particle segregation in dense granular flows, Annu. Rev. Fluid Mech. **50**, 407 (2018).
[4] P. B. Umbanhowar, R. M. Lueptow, and J. M. Ottino, Modeling segregation in granular flows, Annu. Rev. Chem. Biomol. Eng. **10**, 129 (2019).
[5] H. Henein, J. K. Brimacombe, and A. P. Watkinson, Experimental study of transverse bed motion in rotary kilns, Metall. Trans. B **14**, 191 (1983).
[6] J. Mellmann, The transverse motion of solids in rotating cylinders-forms of motion and transition behavior, Powder Technol. **118**, 251 (2001).
[7] E. Clément, J. Rajchenbach, and J. Duran, Mixing of a granular material in a bidimensional rotating drum, Europhys. Lett. **30**, 7 (1995).
[8] F. Cantelaube and D. Bideau, Radial segregation in a 2d drum: An experimental analysis, Europhys. Lett. **30**, 133 (1995).
[9] N. Jain, J. M. Ottino, and R. M. Lueptow, Regimes of segregation and mixing in combined size and density granular systems: An experimental study, Granul. Matter **7**, 69 (2005).
[10] I. Zuriguel, J. M. N. T. Gray, J. Peixinho, and T. Mullin, Pattern selection by a granular wave in a rotating drum, Phys. Rev. E **73**, 061302 (2006).
[11] J. M. N. T. Gray and C. Ancey, Multi-component particle-size segregation in shallow granular avalanches, J. Fluid Mech. **678**, 535 (2011).

[12] C. P. Schlick, Y. Fan, P. B. Umbanhowar, J. M. Ottino, and R. M. Lueptow, Granular segregation in circular tumblers: Theoretical model and scaling laws, J. Fluid Mech. **765**, 632 (2015).
[13] K. M. Hill, D. V. Khakhar, J. F. Gilchrist, J. J. McCarthy, and J. M. Ottino, Segregation-driven organization in chaotic granular flows, Proc. Natl. Acad. Sci. (USA) **96**, 11701 (1999).
[14] D. V. Khakhar, J. J. McCarthy, J. F. Gilchrist, and J. M. Ottino, Chaotic mixing of granular materials in two-dimensional tumbling mixers, Chaos **9**, 195 (1999).
[15] K. M. Hill, G. Gioia, and D. Amaravadi, Radial Segregation Patterns in Rotating Granular Mixtures: Waviness Selection, Phys. Rev. Lett. **93**, 224301 (2004).
[16] K. M. Hill, G. Gioia, D. Amaravadi, and C. Winter, Moon patterns, sun patterns, and wave breaking in rotating granular mixtures, Complexity **10**, 79 (2005).
[17] S. J. Fiedor and J. M. Ottino, Mixing and segregation of granular matter: Multi-lobe formation in time-periodic flows, J. Fluid Mech. **533**, 223 (2005).
[18] J. M. N. T. Gray and V. A. Chugunov, Particle-size segregation and diffusive remixing in shallow granular avalanches, J. Fluid Mech. **569**, 365 (2006).
[19] S. W. Meier, D. A. M. Barreiro, J. M. Ottino, and R. M. Lueptow, Coarsening of granular segregation patterns in quasi-two-dimensional tumblers, Nat. Phys. **4**, 244 (2008).
[20] S. W. Meier, S. E. Cisar, R. M. Lueptow, and J. M. Ottino, Capturing patterns and symmetries in chaotic granular flow, Phys. Rev. E **74**, 031310 (2006).
[21] G. Juarez, R. M. Lueptow, J. M. Ottino, R. Sturman, and S. Wiggins, Mixing by cutting and shuffling, Europhys. Lett. **91**, 20003 (2010).
[22] S. W. Meier, R. M. Lueptow, and J. M. Ottino, A dynamical systems approach to mixing and segregation of granular materials in tumblers, Adv. Phys. **56**, 757 (2007).
[23] I. C. Christov, R. M. Lueptow, J. M. Ottino, and R. Sturman, A study in three-dimensional chaotic dynamics: Granular flow and transport in a bi-axial spherical tumbler, SIAM J. Appl. Dyn. Syst. **13**, 901 (2014).
[24] T. F. Lynn, L. D. Smith, J. M. Ottino, P. B. Umbanhowar, and R. M. Lueptow, Cutting and shuffling a hemisphere: Nonorthogonal axes, Phys. Rev. E **99**, 032204 (2019).
[25] Z. Zaman, M. Yu, P. P. Park, J. M. Ottino, R. M. Lueptow, and P. B. Umbanhowar, Persistent structures in a three-dimensional dynamical system with flowing and non-flowing regions, Nat. Commun. **9**, 3122 (2018).
[26] G. Juarez, I. C. Christov, J. M. Ottino, and R. M. Lueptow, Mixing by cutting and shuffling 3d granular flow in spherical tumblers, Chem. Eng. Sci. **73**, 195 (2012).
[27] P. P. Park, P. B. Umbanhowar, J. M. Ottino, and R. M. Lueptow, Mixing with piecewise isometries on a hemispherical shell, Chaos **26**, 073115 (2016).
[28] P. P. Park, T. F. Lynn, P. B. Umbanhowar, J. M. Ottino, and R. M. Lueptow, Mixing and the fractal geometry of piecewise isometries, Phys. Rev. E **95**, 042208 (2017).
[29] L. D. Smith, P. P. Park, P. B. Umbanhowar, J. M. Ottino, and R. M. Lueptow, Predicting mixing via resonances: Application to spherical piecewise isometries, Phys. Rev. E **95**, 062210 (2017).
[30] T. F. Lynn, J. M. Ottino, P. B. Umbanhowar, and R. M. Lueptow, Identifying invariant ergodic subsets and barriers to mixing by cutting and shuffling: Study in a birotated hemisphere, Phys. Rev. E **101**, 012204 (2020).
[31] S. H. Strogatz, *Nonlinear Dynamics and Chaos: With Applications to Physics, Biology, Chemistry, and Engineering*, 2nd ed., Studies in Nonlinearity (CRC, Boca Raton, FL, 2014).
[32] M. Yu, P. B. Umbanhowar, J. M. Ottino, and R. M. Lueptow, Pattern formation in a fully three-dimensional segregating granular flow, Phys. Rev. E **99**, 062905 (2019).
[33] Z. Zaman, U. D'Ortona, P. B. Umbanhowar, J. M. Ottino, and R. M. Lueptow, Slow axial drift in three-dimensional granular tumbler flow, Phys. Rev. E **88**, 012208 (2013).
[34] See the Supplemental Material at http://link.aps.org/supplemental/10.1103/PhysRevE.106.024902 for a video showing the time resolved development of a large particle segregation pattern in DEM simulation over 30 iterations of the (57°, 57°) tumbling protocol.
[35] J. Rajchenbach, Flow in Powders: From Discrete Avalanches to Continuous Regime, Phys. Rev. Lett. **65**, 2221 (1990).
[36] POV-Ray, the persistence of vision raytracer, http://www.povray.org/ (cited August 2020).
[37] L. D. Smith, P. B. Umbanhowar, J. M. Ottino, and R. M. Lueptow, Mixing and transport from combined stretching-and-folding and cutting-and-shuffling, Phys. Rev. E **96**, 042213 (2017).
[38] J. P. Snyder, Map projections: A working manual, U.S. Geological Survey Professional Paper 1395, Supersedes USGS Bulletin No. 1532 (U.S. Government Printing Office, Washington, D.C., 1987).
[39] L. Wan, T.-T. Wong, and C.-S. Leung, Isocube: Exploiting the cubemap dardware, IEEE T. Vis. Comput. Gr. **13**, 720 (2007).
[40] J. Bridgwater, Self-diffusion coefficients in deforming powders, Powder Technol. **25**, 129 (1980).
[41] B. Utter and R. P. Behringer, Self-diffusion in dense granular shear flows, Phys. Rev. E **69**, 031308 (2004).
[42] A. M. Fry, P. B. Umbanhowar, J. M. Ottino, and R. M. Lueptow, Diffusion, mixing, and segregation in confined granular flows, AIChE J. **65**, 875 (2019).
[43] U. D'Ortona, N. Thomas, Z. Zaman, and R. M. Lueptow, Influence of rough and smooth walls on macroscale flows in tumblers, Phys. Rev. E **92**, 062202 (2015).
[44] The four parameters used to calculate Pe for the MCM computations are $\langle|v_{ax}|\rangle = 1.5$ mm/s, $\sigma_{ax} = 22.1$ mm/s, $L_{island} = 10$ mm, and $\Delta t = 1.6 \times 10^{-4}$ s, where all but the last are obtained from the DEM-derived axial velocity field used in the MCM computations.
[45] C. P. Schlick, Y. Fan, A. B. Isner, P. B. Umbanhowar, J. M. Ottino, and R. M. Lueptow, Modeling segregation of bidisperse granular materials using physical control parameters in the quasi-2D bounded heap, AIChE J. **61**, 1524 (2015).
[46] H. Xiao, P. B. Umbanhowar, M. J. Ottino, and R. M. Lueptow, Modelling density segregation in flowing bidisperse granular materials, Proc. R. Soc. A **472**, 20150856 (2016).
[47] The smaller concentration of low-density particles in these density-bidisperse mixtures compared to the concentration of large particles in the size-bidisperse mixtures reflects the fact that a volume of 2 mm low-density particles occupies a larger surface area on the tumbler wall than an equal volume of 4 mm

particles. Therefore, in order to avoid covering the entire surface with light particles and to reveal potential segregation patterns, light particle concentrations need to be smaller.

[48] U. D'Ortona, N. Thomas, and R. M. Lueptow, Influence of rough and smooth walls on macroscale granular segregation patterns, Phys. Rev. E **93**, 022906 (2016).

[49] J. Bridgwater, Mixing of powders and granular materials by mechanical means—A perspective, Particuology **10**, 397 (2012).

[50] M. Marigo, M. Davies, T. Leadbeater, D. L. Cairns, A. Ingram, and E. H. Stitt, Application of positron emission particle tracking (PEPT) to validate a discrete element method (DEM) model of granular flow and mixing in the Turbula mixer, Int. J. Pharm. **446**, 46 (2013).

[51] C. Mayer-Laigle, C. Gatumel, and H. Berthiaux, Mixing dynamics for easy flowing powders in a lab scale Turbula® mixer, Chem. Eng. Res. Des. **95**, 248 (2015).

[52] J. M. Ottino, *The Kinematics of Mixing: Stretching, Chaos, and Transport* (Cambridge University Press, Cambridge, 1989).

[53] L. D. Smith, M. Rudman, D. R. Lester, and G. Metcalfe, Bifurcations and degenerate periodic points in a three dimensional chaotic fluid flow, Chaos **26**, 053106 (2016).

[54] J. Moser, *Stable and Random Motions in Dynamical Systems* (Princeton University Press, Princeton, NJ, 1973).

[55] P. A. Cundall and O. D. L. Strack, A discrete numerical model for granular assemblies, Géotechnique **29**, 47 (1979).

[56] J. Shäfer, S. Dippel, and D. Wolf, Force schemes in simulations of granular materials, J. Phys. I France **6**, 5 (1996).

[57] L. E. Silbert, G. S. Grest, R. Brewster, and A. J. Levine, Rheology and Contact Lifetimes in Dense Granular Flows, Phys. Rev. Lett. **99**, 068002 (2007).

[58] G. H. Ristow, *Pattern Formation in Granular Materials* (Springer, Berlin, 2000).

[59] Y. Fan, P. B. Umbanhowar, J. M. Ottino, and R. M. Lueptow, Kinematics of monodisperse and bidisperse granular flows in quasi-two-dimensional bounded heaps, Proc. R. Soc. A **469**, 20130235 (2013).